LAWRENCE
LIVERMORE
NATIONAL
LABORATORY

LLNL-CONF-577732

The Gemini Planet Imager: Integration and Test

B. A. Macintosh

August 29, 2012

SPIE Astronomical Instrumentation 2012
Amsterdam, Netherlands
July 1, 2012 through July 7, 2012

Disclaimer

The Gemini Planet Imager: Integration and Test

Bruce A. Macintosh[a], Andre Anthony[h], Jenny Atwood[h], Nicolas Barriga[b], Brian Bauman [a], Kris Caputa[h], Jeffery Chilcote[f], Daren Dillon[c], René Doyon[d], Jennifer Dunn[h], Donald T. Gavel[e], Ramon Galvez[b], Stephen Goodsell[b], James R. Graham[ci], Markus Hartung[b], Joshua Isaacs[l], Dan Kerley[h], Quinn Konopacky[k], Kathleen Labrie[b], James Larkin[f], Jerome Maire[k], Christian Marois [h], Max Millar-Blanchaer[k], Arturo Nunez[b], Ben Oppenheimer[g], David Palmer[a], John Pazder[h], Marshall Perrin[j], Lisa A. Poyneer [a], Carlos Quiroz[b], Fredrik Rantakyro[b], Vlad Reshtov[h], Les Saddlemyer[h], Naru Sadakuni[c], Dmitry Savransky[a], Anand Sivaramakrishnan[j], Malcolm Smith[h], Remi Soummer [j], Sandrine Thomas[b], J. Kent Wallace[i], Jason Weiss[f], Sloane Wiktorowicz[c]
[a]Lawrence Livermore National Laboratory, 7000 East Ave., L-210, Livermore, CA 94040; [b]Gemini Observatory, Hilo, HI 96720;
[c]Department of Astronomy, University of California at Berkeley, Berkeley, CA 94720
[d]Universite de Montreal, Department de Physique, Montreal, QC, H3C 3J7, Canada
[e]UC Santa Cruz, 1156 High Street, Santa Cruz, CA
[f]Department of Physics and Astronomy, UC Los Angeles, Los Angeles, CA 90095
[g]Department of Astrophysics, American Museum of Natural History, New York, NY 10024
[h]Herzberg Institute of Astrophysics, 5071 West Saanich Road, Victoria, BC V8X 4M6
[i]Jet Propulsion Laboratory, California Institute of Technology, Pasadena, CA 91109; [j]Space Telescope Science Institute, Baltimore, MD 21218; [k]Dunlap Institute, University of Toronto, Toronto, ON M5S 3H4 [l]University of Wisconsin, Madison WI 53706

ABSTRACT

The Gemini Planet Imager is a next-generation instrument for the direct detection and characterization of young warm exoplanets, designed to be an order of magnitude more sensitive than existing facilities. It combines a 1700-actuator adaptive optics system, an apodized-pupil Lyot coronagraph, a precision interferometric infrared wavefront sensor, and a integral field spectrograph. All hardware and software subsystems are now complete and undergoing integration and test at UC Santa Cruz. We will present test results on each subsystem and the results of end-to-end testing. In laboratory testing, GPI has achieved a raw contrast (without post-processing) of 10^{-6} 5σ at 0.4", and with multiwavelength speckle suppression, $2x10^{-7}$ at the same separation.

Keywords: Adaptive optics; extrasolar planets; coronagraphy; integral field spectrograph

1. INTRODUCTION

Since 1995, the study of extrasolar planets has become one of the most active areas of astronomy. Precision Doppler measurements rapidly led to the discovery of dozens of planetary systems – all of them with architectures radically different than our own, dominated by giant planets much closer to their star than expected. Then, the first detections of transits opened up extrasolar planets to characterization – initially by providing measurements of mass and radius, and ultimately through measurements of planetary spectra in transit and eclipse. The *Kepler* spacecraft is now providing thousands of candidate and confirmed transiting planets and approaching the detection of Earth analogs.

These impressive discoveries have left the theory of planet formation in some disarray, with no consensus model that explains all the properties of known systems. One unexplored piece of the puzzle is the frequency and properties of planets in the 5-40 AU regime, where the giant planets in our solar system reside and where giant planets are thought to form; a region almost inaccessible to Doppler and transit techniques. It is probed by gravitational microlensing but only in a broad statistical sense. Direct imaging with current-generation AO systems is most sensitive beyond 40 AU – it has led to a handful of significant discoveries[12], but too few planets to paint a systematic and comprehensive picture. Moving beyond this requires dedicated instruments optimized for exoplanet imaging, capable of achieving contrasts of 10^6 to 10^7

at separations of 0.4" or less. Instruments such as SPHERE[3], P1640[4], and the Gemini Planet Imager (GPI) will provide this capability.

Macintosh et al.[5] discusses the scientific requirements of GPI in more detail, and its overall design. McBride et al[6] simulations of its science reach. Here we discuss the basic design of GPI, the performance of its subsystems, integration and test status, and end-to-end performance testing.

1.1 Overview of the GPI design

The Gemini Planet Imager consists of seven major subsystems. The adaptive optics (AO) system, measures fast atmospheric wavefront errors and corrects them using a pair of deformable mirrors. The calibration wavefront sensor (CAL) provides time-averaged measurements of the infrared wavefront at high precision and feeds those back to the main AO system. The integral field spectrograph (IFS) takes near-infrared spectra or polarization measurements over the science field of view. The apodized-pupil Lyot coronagraph (COR) consists of diffraction-blocking masks located within the other three subsystems. The parts are held together by the opto-mechanical subsystem (OMSS). A top-level computer (TLC) software layer provides control, connection, and interfaces with the observatory. Finally, a data reduction pipeline (DRP) reconstructs raw IFS images into three-dimensional data cubes.

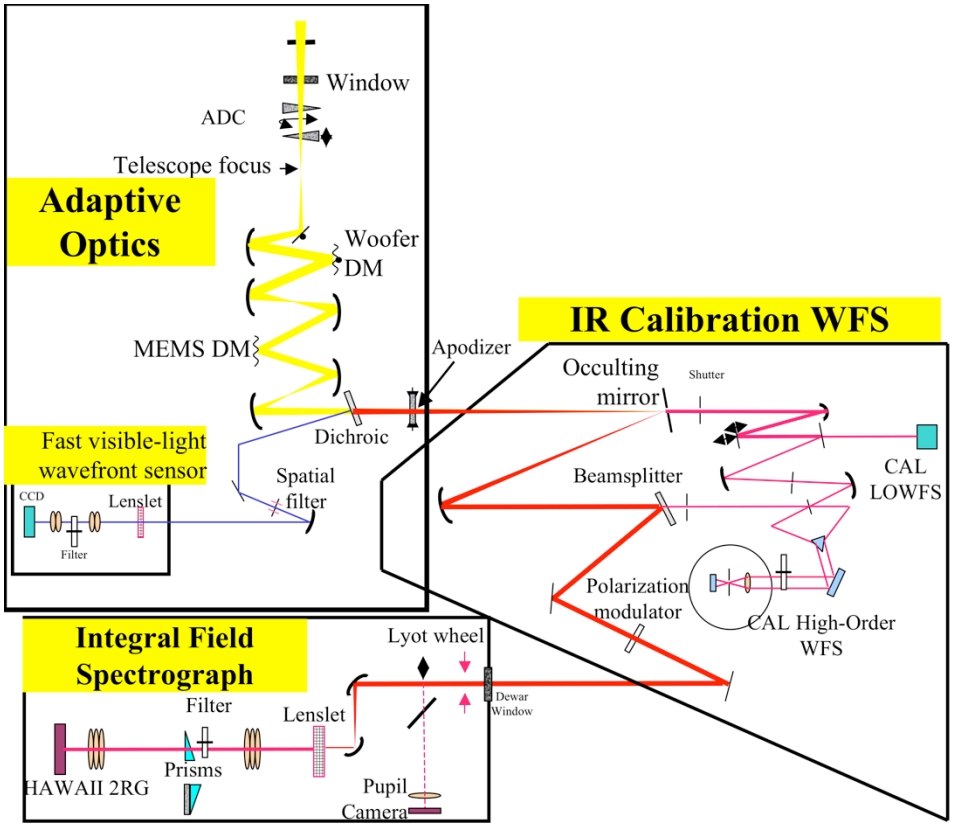

Figure 1: Schematic of GPI showing key subsystems.

2. SUBSYSTEMS TIMELINE AND STATUS

All subsystems have been delivered to the integration and test (I&T) site at UC Santa Cruz by January 2012. We discuss their capabilities and status briefly here.

2.1 Adaptive optics

The adaptive optics (AO) system was developed by the Lawrence Livermore National Laboratory. It uses a spatially-filtered Shack-Hartmann wavefront sensor to measure the incoming wavefront at up to 1.2 kHz. The sensor uses a 160x160 pixel Lincoln Labs CCID-66 device (only the inner 128x128 pixels are read.) Readnoise was measured at ~3 electrons in early testing, and is ~5 electrons after integration into the GPI bench. Each subaperture corresponds to a 2x2 pixel quad cell with a 1-pixel guard band (See Figure 4 for a WFS image.) The subsystem was tested with surrogate optics at LLNL in 2010, and integrated into the OMSS in early 2011.

Wavefronts are reconstructed with a Fourier-transform algorithm[7] by the adaptive optics computer (AOC), a 16-core Dell server running real-time Linux. The AO code is highly reliable and provides access to a wide variety of telemetry continuously at the full update rate. Typical delay from the end of a frame read to the application of a correction on the DM is 590 microseconds. The system is typically operated at 1 kHz - an adaptive modal controller automatically adjusts loop gains, rather than frame rate, to improve performance on brighter or dimmer stars. The corrections are applied by two deformable mirrors. The "woofer" is a low-order (N=9) piezoelectric DM constructed by CILAS. The "tweeter" is a 64x64 silicon MEMS deformable mirror[8] from Boston Micromachines. The GPI pupil has a diameter of 43.2 subapertures (18 cm in size) on the Gemini South telescope, so only a 44-actuator-radius circle on the DM is fully controlled. However, even after multiple foundry runs, no MEMS was available without at least some defective actuators within the GPI pupil. By carefully selecting the operating region, however, we were able to locate a region where all bad actuators are located at the edges of the pupil or behind the secondary mirror obscuration. A single bad actuator can have an enormous impact on final contrast, spraying light throughout the dark hole high-contrast region. However, this scattered light is well-confined in the Lyot plane[9] to the region of the bad actuators themselves. A customized lyot mask with individual tabs can block that light, restoring almost all the full contrast (Figure 2).

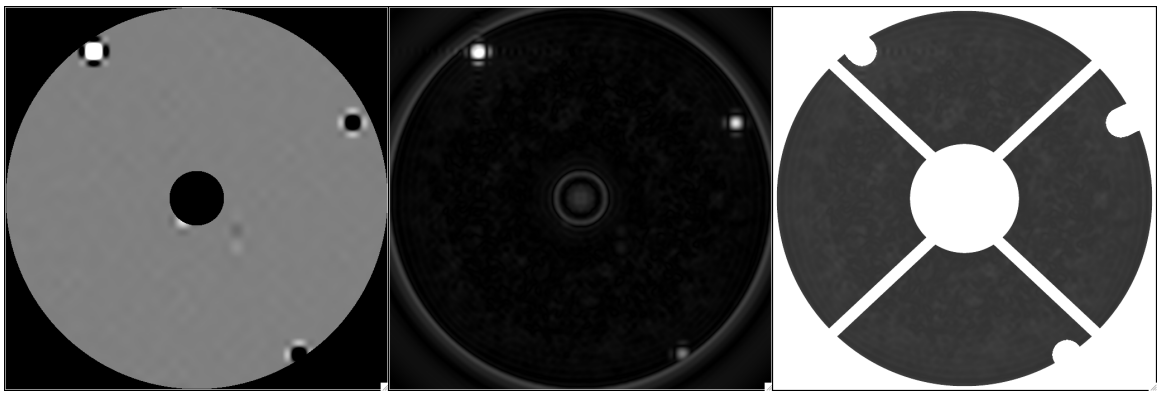

Figure 2: Left: Phase map of the MEMS showing three defective actuators. Center: Intensity in the Lyot plane of the coronagraph. Right: Custom Lyot mask blocking the bad actuators.

The subapertures surrounding the bad actuators are masked out of the overall wavefront reconstruction. Passing through the spatial filter, light from the bad actuators also biases the phase measurements in nearby subapertures; optimization of the control-loop properties, particularly the integrators, for those actuators is necessary to improve the stability of the system.

Fine alignment of the AO WFS was especially challenging. The WFS lenslets have a pitch of 63 microns and a focal length of 1mm (reimaged to 3 CCD pixels by a 1:1 relay), resulting in a Fresnel number (after the lenslets) of ~5. At such a low number waveoptics effects are significant; for example, the Z distance resulting peak intensity on the WFS CCD is displaced from the true focus[10], while the Talbot effect can cause intensity variations on the CCD if it is mis-conjugated to the DM by even 1 mm. The WFS had to be aligned with a high-resolution camera and precise metrology before installation of the CCID66 detector.

The adaptive optics system has undergone extensive testing with rotating phase plates to simulate atmospheric turbulence[11]. Poyneer[12] reports on early testing. Closed-loop performance shows that the system can be operated in nominal configuration down to I=8 mag and remains stable on I=10 mag with the spatial filter opened.

After more than 1 year of successful operation, the science-grade MEMS device suffered a single actuator failure on May 29 2012. The actuator failure occurred after the AO realtime computer was rebooted while the MEMS drivers were

powered on. This often results in a lockup of communication between the MEMS and AOC, setting actuators to random voltages. The mirror was then left in this state for approximately 8 hours before the driver power was cycled. Since the damage threshold for the MEMS is ~230 V and the driver power supply is hardware-limited to 205 V it is unclear how this led to an actuator failure; a transient during the reboot or a fluctuation on the supply lines or ground during the lockup period are possibilities. Pre-ship testing data, including IR microscopy that examine the interior of the MEMS, showed no previous evidence of a defect. We have put procedures in place to avoid these circumstances in the future, so that the MEMS is only powered when the AOC computer is operational, but this remains a concern. One spare science-grade MEMS of similar quality is available, and Boston Micromachines and Boston University are developing next-generation MEMS expected to have higher yields.

The damaged actuator is stuck near the mirror bias level, and is only intermittently responsive to voltage, and somewhat responsive to movement of adjacent actuators. Adjusting the bias of the whole device by ~60 V moves the rest of the device to match the actuator and allowed the MEMS to be flattened. This mode was used for high-contrast testing described in Section 3 but unacceptably reduces total stroke. The failed actuator will be blocked with an additional tab in the Lyot plane.

2.2 OMSS and AO optics

The opto-mechanical super structure (OMSS) was constructed by the Herzberg Institute of Astrophysics in Canada. It consists of a mounting plate that connects to the Gemini Cassegrain instrument mount, a custom optics bench to hold the AO components, and a truss structure coming off from the mounting plate to hold the three major subsystems (AO, CAL and IFS).

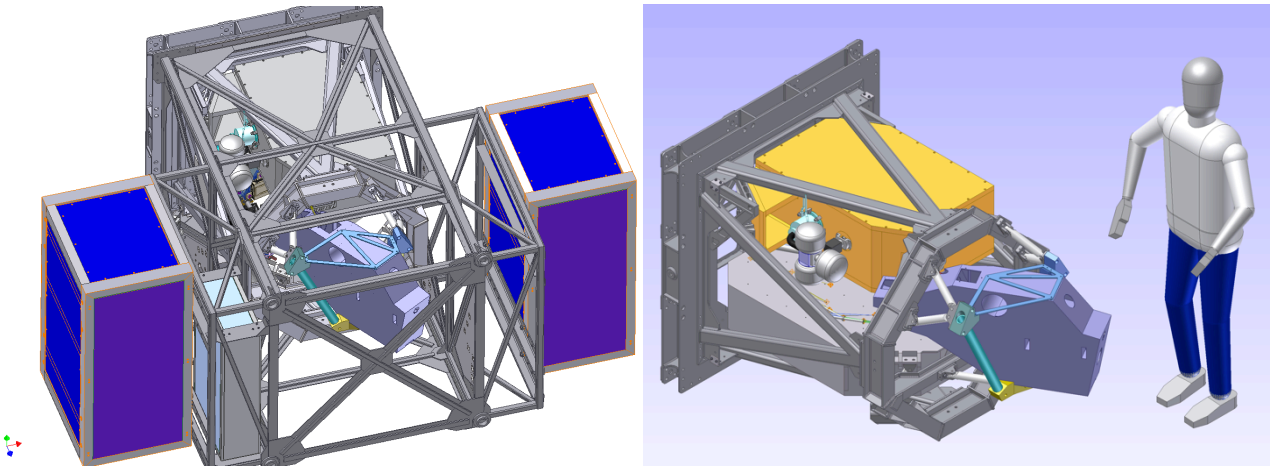

Figure 3: Mechanical design of the Gemini Planet Imager. Left: GPI with its covers removed, showing the outer frame structure and electronics racks and the inner FSS. Right: Flexure Sensitive Structure (FSS) with the optical subsystems. The IFS is the yellow dewar at top; the CAL interferometer is inside the blue box at right (the final mounting uses a different bipod arrangement than shown here); the AO subsystem is mounted on the grey optical bench at bottom. The square plate on the left mounts to the Gemini Cassegrain Instrument Support Structure.

The AO relay uses two matched pairs of off-axis parabolas to locate the telescope pupil on the deformable mirrors (both conjugate to the ground) and an off-axis ellipse to produce an f/64 output beam with a pupil located in the converging space. These optics were polished by Precision Asphere of Fremont California to < 1 nm RMS wavefront error at mid spatial frequencies, a requirement driven by GPI's high-contrast needs[13]. The optical train was aligned using commercial small Shack-Hartmann wavefront sensors to < 13 nm RMS WFE from the input cassegrain focus to the output pupil[14].

After assembly, the OMSS was flexure-tested by HIA using surrogate weights and sensors in place of the CAL and IFS subsystems. Typical flexures were < 25 microns over 180 degree rotations, well within specification.

After testing, the OMSS was shipped from HIA to UC Santa Cruz in December 2010.

2.3 CAL

The calibration interferometer / wavefront sensors (CAL) subsystem is intended to address the problem of non-common-path (NCP) aberrations – optical errors that occur after the spilt between the wavefront sensor and science path and

hence are either unsensed or inappropriately corrected. In the case of a coronagraph, the key location is the focal plane mask – small optical errors after that location have little effect on contrast.

The CAL subsystem is designed to measure the wavefront at this location, at near-infrared (1.5-1.7 micron) wavelengths, to sample time and wavelength variations in the NCP errors. Low-order aberrations, including tip and tilt, are measured with a low-order (N=7) Shack-Hartmann sensor (LOWFS) looking through the coronagraph focal plane mask hole. High-order aberrations are measured by a point-diffraction interferometer[15] interfering a fraction of the science-path light with a reference wavefront created using the light that passed through the FPM pinhole. Operating after a coronagraph, the absolute requirements of the interferometer for a given pre-coronagraph measurement precision are much relaxed [5 15]. The CAL system also holds the coronagraph focal plane masks. The CAL system was installed in GPI in October 2011. Commissioning of the CAL module is still in progress; feedback from the LOWFS has been demonstrated to ~5 nm precision, but absolute accuracy is lower, and the interferometer mode, though demonstrated at JPL, has not been integrated into GPI operations. In the current plan, the optimal GPI wavefront will be determined with focal-plane techniques (Section 3), and those used to record a reference wavefront offset for the CAL sensors.

2.4 Coronagraph

GPI uses an apodized-pupil Lyot coronagraph (APLC.)[16] This combines a classic Lyot coronagraph (hard-edged focal-plane occultor and undersized pupil-plane Lyot stop) with a moderate apodization function, matched to the occultor geometry to almost completely attenuate the light within the original pupil diameter. In GPI's case, the apodizers are in a pupil-plane-mask (PPM) wheel located on the adaptive optics bench. The occultors are reflective in design, with the on-axis light sent through a hole while off-axis science light is reflected; these occultors are mounted in a selection wheel in the Calibration subsystem. Finally, the cryogenic Lyot stops are located in a wheel inside the Integral Field Spectrograph.

Apodizers were manufactured with aluminum/chromium microdots, placed using an error diffusion algorithm, on glass substrates[17]. To minimize physical-optics effects, the dot size is 10 microns, though individual. Testing shows these reproduce the target apodization profile to better than 1% accuracy. Although the desired APLC transmission profile is wavelength-independent, small physical optics effects do result in a chromatic transmission on the real masks, so different masks are selected for each wavelength band.

The reflective focal plane masks are thin gold-coated silicon substrates, with the occultor hole etched to 2 micron accuracy[18]. Since the APLC design requires a mask of ~5.6 λ/D for optimal operation, separate masks exist for each of the Y, J, H, and K bands.

2.5 IFS

GPI's science instrument is an integral field spectrograph constructed at UCLA. An IFS is extremely powerful for high-contrast imaging; true companions can be distinguished from speckle artifacts through their chromatic behavior, and companions can be spectrally characterized. The GPI IFS is a lenslet-based design, similar to the Keck OSIRIS instrument. A grid of lenslets in the focal plane dissects the image into a sparse grid of dots with enough space between them that the spectra can then be dispersed by a prism. This gives R~34 in Y band (0.95-1.14 μm) to R~70 in K band, which we divide into two smaller filters (1.90-2.19 μm and 2.13-2.40 μm). Individual spectra are 16 pixels long and separated by 4.5 pixels from their neighbors to reduce crosstalk to acceptable levels. The spatial sampling is 0.014 arcseconds per pixel. This gives a field of view of 2.8x2.8 arcseconds on a HAWAII 2RG detector. The IFS testing is discussed in a separate paper[19]. In polarimetric mode, the spectral prism is replaced with a Wollaston prism that separates the two orthogonal polarizations from each lenslet onto on the final detector. A quarter-wave-plate modulator is located outside the dewar.

Rather than the commonly-used GM-cycle cryocoolers, the IFS uses two Sunpower Stirling-cycle coolers that have lower total vibration. These are self-contained units with no external compressor – when provided with electrical power and cooling water, each has ~15W of cooling power at 60-65K. Their vibration is a very pure sinusoid, with the 60Hz component (damped by a passive counterweight system), and harmonics at 120 and 180 Hz. Although the intrinsic vibration is low, a significant portion of it was coupling into the IFS body and directly into the IFS detector itself, resulting in microphonic noise of tens of electrons equivalent. Improved cooler mountings with damping material have addressed this. In early testing, cryocoolers failed in operation, primarily due to excessive force applied to the cold tip. With modifications to minimize these forces the coolers have been reliable. The IFS was delievered to UCSC and installed in GPI in January 2012.The vibration induced into the GPI AO optical path has been measured at ~6 mas RMS

at 180 Hz, almost certainly a motion in the wavefront sensor leg (which the AO controller can be adjusted to ignore), within specifications.

The IFS also provides a pupil-viewing mode with 200 pixels across the Lyot plane, using a Sensors Unlimited InGaAs camera sensitive from 1.5-1.7 microns. This is a crucial diagnostic for alignment and for evaluating coronagraph performance. Figure 4 shows a first-light pupil image after IFS installation.

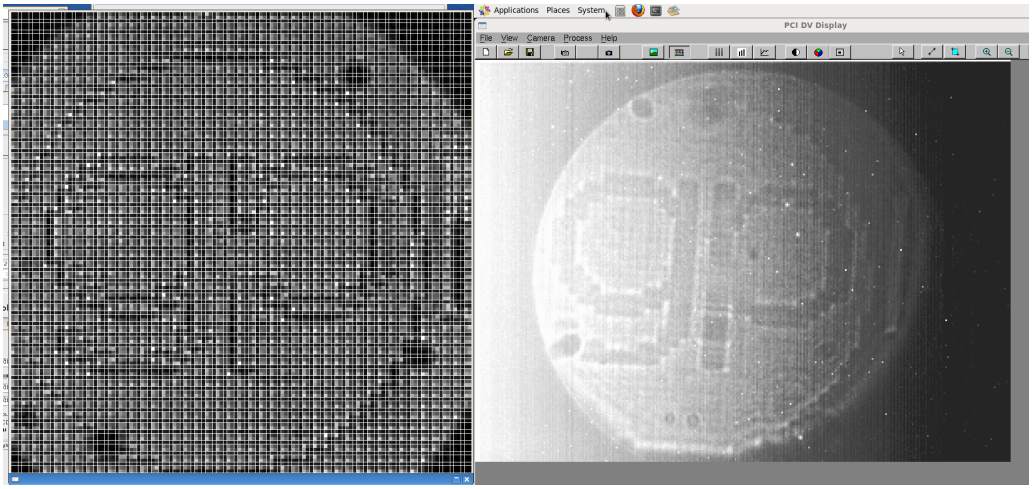

Figure 4: First light on the IFS. Left: GPI wavefront sensor image showing test pattern. Right: IFS pupil image.

2.6 TLC and control software

Communication between the subsystems and the observatory, motion control, and sequencing is provided by the Top Level Computer (TLC) software. Large-scale data exchange with subsystems is done through a shared-memory block. An engineering GUI provides local control; Gemini software engineers are developing the interface to the standardized Gemini Observatory user interfaces. We have also developed interfaces that allow IDL sessions to control most aspects of GPI, allowing complex scripting of alignment or test sequences.

2.7 Data reduction pipeline

The IFS raw images consist of ~40,000 individual microspectra, each 16 pixels long, spread out across the H2RG array. The data reduction pipeline converts these into a 200x200x37 three-dimenstional spectral cube and provides a customized GPItv program to interact with these cubes, including automatic calculation of contrast. Testing shows the pipeline recovers photometry to ~0.6% RMS accuracy and wavelength to less than a pixel. The data pipeline is discussed in a companion paper[20].

3. INTEGRATION AND TEST

GPI is a complex instrument, and integration has been a complex task. We have overcome several significant technical challenges. As discussed above, the IFS Stirling-cycle cryocoolers had several early problems, and alignment of the WFS CCD required its removal from GPI for precise off-bench measurements. Thermal flexure in the WFS was also a problem. Typical pointing tolerance at various locations in the GPI optical train are ~5 miliarcseconds. Most GPI optical spaces are f/64 to f/200 to provide sufficient sampling of the ~40 mas Gemini H-band diffraction limit, so 5 mas translates into 10 micron motion requirements, challenging but feasible. The WFS, however, must encompass the seeing limit or diffraction limit of a single 18cm subaperture, so each WFS pixel is 1 arcsecond – in that space, 5 mas corresponds to 0.1 microns of motion. Measured WFS thermal flexure was 10 mas per degree C, particularly challenging since the I&T environment (the UCSC High Bay) can experience 15C temperature swings in 8 hour periods. Open-loop and closed-loop control can overcome most of this flexure, but it was necessary to put the AO WFS spatial filter on an xy stage to allow it to track the location of the WFS boresight. The spatial filter was also modified to allow it to be irised down to a pinhole to provide a perfect spherical wavefront for calibration of the wavefront sensor reference centroids. Overall, more than a year was spent integrating subsystems and modifying them to operate under integrated conditions.

3.1 Contrast testing

With the final installation and alignment of the IFS, end-to-end contrast testing began. GPI can be fed either by an internal artificial star unit – a Thor Labs NA=0.35 single mode fiber at the input Cassegrain focus – or an external telescope simulator that replicates the Gemini pupil and can include simulated atmospheric turbulence. Both are illuminated by a Fianium Supercontinuum light source; a conventional incandescent source output through the high-NA fibers would correspond to a ~6th magnitude star, which would in turn require hour-long exposures to reach target contrast levels.

The coronagraph apodizer, GPI DM pupil, and Lyot stop were aligned using the IFS pupil-viewing camera and automated IDL codes. The star is centered on the focal plane mask using a dithering algorithm. All contrasts are evaluated by measuring the standard deviation in a series of annuli of width 1 λ/D. They are normalized to the four reference satellite images (see Figure 5) created by a grid designed into the apodizer masks[21 22]. When a single contrast figure is given, it is 5 times this standard deviation, typically at a 0.4" radius if not otherwise stated.) Initial contrast testing showed performance at the 10^{-5} level. This was clearly limited by non-common-path errors. The CAL system is not yet capable of providing an absolute wavefront reference, so these errors had to be mitigated through other techniques. First, the spatial filter pinhole mode was used to provide a spherical calibration wavefront to the wavefront sensor. This corrects for all non-common-path errors in the wavefront sensor leg (particularly the errors in the lenslets themselves.) This improved contrast by a factor of 3.

Next, we deployed a speckle nulling algorithm[23 24]. Briefly, this operates by identifying the brightest speckles (typically 100 per iteration) in the focal plane. To first order, each speckle corresponds to a single Fourier component of the phase[25]. The algorithm applies a test sequence of the corresponding Fourier components at various phases, then computes the optimal correction to remove the speckle. The process repeats on the brightest remaining speckle. In 3-6 iterations, this improved contrast below 10^{-6}. Contrast at small radii (<0.4") is limited by coronagraph leakage caused by low-order aberrations and is hence difficult for speckle nulling to correct. Other strategies, such as classical focus diversity, will be used to control these effects.

GPI was designed from the beginning to minimize PSF chromaticity. The residual speckles are very well behaved as a function of wavelength. As a result, a simple spectral differencing algorithm[26] applied to the IFS cubes achieves a contrast of 1.5×10^{-7} (5σ), nearly reaching the original design requirement.

Figure 5 shows the contrast vs radius through these experiments. In each case, no external aberrations (e.g. simulated atmospheric turbulence) was included, so this represents a contrast floor – additional noise from atmospheric speckles or stellar halo photon noise will of course further reduce contrast. This internal contrast ratio represents the fundamental limit that GPI could achieve regardless of the brightness of a star. Since such systematic and quasi-static errors completely dominate high-contrast imaging with current systems, far beyond photon or atmospheric-speckle noise, this is the best figure of merit for early testing of a high-contrast imager. Wavefront control strategies and testing are further discussed in a companion paper[27].

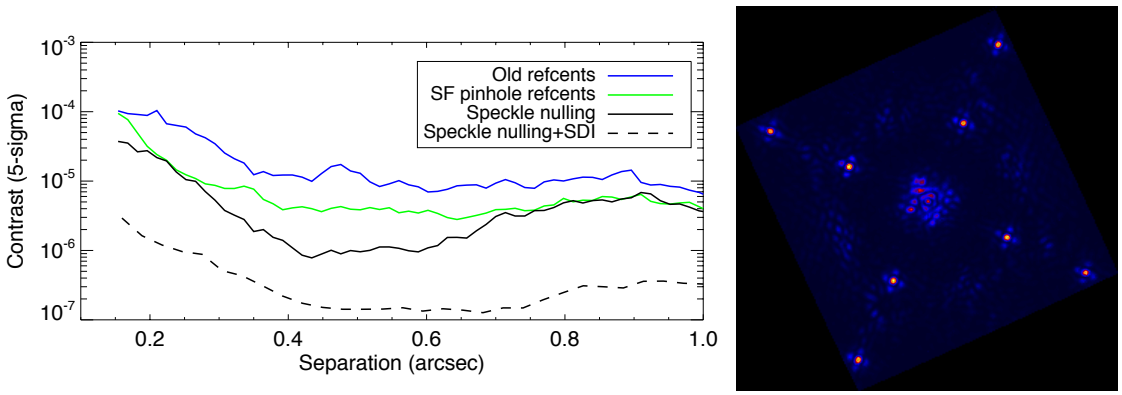

Figure 5: Left: Contrast (5σ speckle noise) vs radius in closed-loop GPI testing, with no external aberrations. The light source represents a bright (H~3 mag) star. Top curve shows contrast with WFS reference centroids generated using an optical fiber during final alignment. The next curve shows contrast with WFS reference centroids generated immediately before the nulling experiment using the spatial filter pinhole mode. The bottom solid curve shows the contrast after speckle

nulling. The dashed curve shows the same data set with a simple multiwavelength spectral differencing algorithm applied to the IFS channels. Right (Video 1): IFS image, 2.8 arcseconds on a side. The two sets of four reference spots generated by the apodizer grid can be seen at 1:00, 4:00, 7:00, and 10:00. http://dx.doi.org/doi.number.goes.here

4. CONCLUSIONS AND FUTURE STEPS

Due to the actuator failure, the instrument will require at least one more IFS warmup and cooldown cycle to install the upgraded Lyot masks, as well as final performance optimization and the development of operational procedures (such as fully automated calibration and alignment.) It is expected that formal acceptance testing will begin before the end of 2012, with the instrument shipping to Chile in the first half of 2013. First light on GPI (and its competitors) will open up a new, unexplored volume of the universe – the region within a few AU of bright stars – to a wide variety of science missions. The core exoplanet survey will survey 600 stars over 890 hours of telescope time and is sensitive to true Jupiter analogs (1 Jupiter mass at 5 AU) around nearby young stars. GPI will also be open of a variety of PI science - ranging from polarimetric imaging of young protoplanetary disks to high-contrast studies of the outflow from post-main-sequence stars. GPI and its competitors should revolutionize our understanding of other solar systems.

5. ACKNOWLEDGEMENTS

Portions of this workwere performed under the auspices of the U.S. Department of Energy by Lawrence Livermore National Laboratory under Contract DE-AC52-07NA27344.

REFERENCES

[1] Marois, C., et al, “Direct imaging of multiple planets orbiting a star,” Science 322, 1348 (2008)
[2] LaGrange, A.-M., et al., “A giant planet imaged in the disk of the young star β Pictoris,” Science 329, 57 (2010)
[3] Beuzit, J.-L., et al., “SPHERE: A planet finder instrument for the VLT,” Proc. SPIE 7014, 70148 (2008)
[4] Oppenheimer, B., et al., “Project 1640: The world’s first ExAO coronagraphic hyperspectral imager for comparative planetary science,” Proc. SPIE 8447 (2012)
[5] Macintosh, B., et al., “The Gemini Planet Imager: from science to design to contruction,” Proc. SPIE 7015, 701518 (2008)
[6] McBride, J., et al, “Experimental design for the Gemini Planet Imager,” PASP 123, 692 (2011)
[7] Poyneer, L., Gavel, D., and Brase, J., “Fast wave-front reconstruction in large adaptive optics systems with use of the Fourier transform,” JOSA A 19, 2100 (2002)
[8] Cornelissen, S., Bierden, P., and Bifano, T., “A 4096 element continuous facesheet MEMS deformable mirror for high-contrast imaging,” Proc. SPIE 6888, 68880V (2008)
[9] Sivaramakrishnan, A., Lloyd, J.P., “Spiders in Lyot Coronagraphs,” Ap.J., 633, 528 (2005)
[10] Baranec, C., “Design considerations for low-light level low-Fresnel number optical systems,” Applied Optics 48, 6259 (2009)
[11] Rampy, R., et al., “New method of fabricating phase screens for simulated atmospheric turbulence,” Proc. SPIE 7736, 77362Y (2010)
[12] Poyneer, L., et al., “The use of a high-order MEMS deformable mirror in the Gemini Planet Imager,” Proc. SPIE 7931, 793104 (2011)
[13] Marois, C., et al., “An end-to-end polychromatic Fresnel propagation model of GPI,” Proc. SPIE 7015, 10151T (2008)
[14] Pazder, J., et al. “The optical alignment of the Gemini Planet Imager adaptive optics bench”, Proc. SPIE 8450 (2012)
[15] Wallace, J.K., et al., “The Gemini Planet Imager calibration wavefront sensor instrument,” Proc.SPIE 7736, 77365D (2010)
[16] Soummer, R., et al., “Apodized pupil Lyot coronagraphs for arbitrary apertures. III. Quasi-achromatic solutions,” Ap.J. 729, 244 (2011)
[17] Sivaramakrishnan, A. et al., "Calibrating IR optical densities for the Gemini Planet Imager extreme adaptive optics coronagraph apodizers," Proc. SPIE 7440 (2009)
[18] Sivaramakrishnan, A., et al., "Gemini Planet Imager coronagraph testbed results," Proc. SPIE 7735 (2010)

[19] Chilcote, J., et al., “Performance of the integral field spectrograph for the Gemini Planet Imager,” Proc. SPIE 8446, (2012)
[20] Maire, J., et al., “Test results for the Gemini Planet Imager data reduction pipeline,” Proc. SPIE 8451 (2012)
[21] Marois, C., et al., “Accurate astrometry and photometry of saturated and coronagraphic point spread functions,” Ap.J. 647, 612 (2006)
[22] Sivaramakrishnan, A., and Oppenheimer, B., et al., “Astrometry and photometry with coronagraphs,” Ap.J., 647, 620 (2006)
[23] Savransky, D., et al., “Focal plane wavefront sensing and control for ground-based imaging,” Proc. SPIE 8447 (2012)
[24] Trauger, J., and Traub, W., “A laboratory demonstration of the capability to image an Earth-like extrasolar planet,” Nature 446, 771
[25] Perrin, M., et al, “The structure of high Strehl ratio point spread functions,” Ap.J. 596, 702 (2003)
[26] Marois, C., et al., “Efficient speckle noise attenuation in faint companion imaging,” PASP 112, 91 (2000)
[27] Thomas, S., et al., “Wavefront control strategies for the Gemini Planet Imager,”,Proc. SPIE 8447 (2012)